JCTC Journal of Chemical Theory and Computation

Article

Cite This: J. Chem. Theory Comput. 2019, 15, 6074−6084

pubs.acs.org/JCTC

Locating Minimum Energy Crossings of Different Spin States Using the Fragment Molecular Orbital Method

Danil S. Kaliakin,[†,∥] Dmitri G. Fedorov,[‡] Yuri Alexeev,[§] and Sergey A. Varganov*[,†]

[†]Department of Chemistry, University of Nevada, Reno, 1664 N. Virginia Street, Reno, Nevada 89557-0216, United States

[‡]Research Center for Computational Design of Advanced Functional Materials (CD-FMat), National Institute of Advanced Industrial Science and Technology (AIST), Central 2, Umezono 1-1-1, Tsukuba 305-8568, Japan

[§]Computational Science Division and Argonne Leadership Computing Facility, Argonne National Laboratory, Argonne, Illinois 60439, United States

Supporting Information

ABSTRACT: Spin-dependent processes involving nonadiabatic transitions between electronic states with different spin multiplicities play important roles in the chemistry of complex systems. The rates of these processes can be predicted based on the molecular properties at the minimum energy crossing point (MECP) between electronic states. We present the development of the MECP search technique within the fragment molecular orbital (FMO) method applicable to large complex systems. The accuracy and scalability of the new method is demonstrated on several models of the metal−sulfur protein rubredoxin. The effect of the model size on the MECP geometry and relative energy is discussed. The fragment energy decomposition and spin density delocalization analyses reveal how different protein residues and solvent molecules contribute to stabilization of the spin states. The developed FMO-MECP method can help to clarify the role of nonadiabatic spin-dependent processes in complex systems and can be used for designing mutations aimed at controlling these processes in metalloproteins, including spin-dependent catalysis and electron transfer.

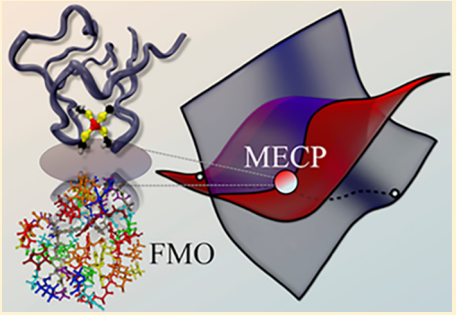

I. INTRODUCTION

Nonadiabatic processes involving nonradiative transitions between different electronic states play important roles in broad areas of chemistry and biology. Examples include combustion,[1,2] reactions in planetary atmospheres and interstellar space,[3,4] transition-metal-based catalysis,[5] binding of small molecules to the active sites of metalloproteins,[6−9] visual perception,[10,11] and protection against UV light in living organisms.[12−17] Spin-forbidden nonradiative transitions between electronic states of different spin multiplicities are called intersystem crossings (ISCs).[12,18,19] The rates of ISCs can be predicted either with statistical theories or nonadiabatic molecular dynamics (NA-MD). For small systems, the NA-MD approach is preferable because it can sample complex features of the potential energy surfaces (PESs) and account for ISC transitions anywhere on these surfaces. However, due to the computational demands, the NA-MD methods, such as ab initio multiple spawning[20−23] and trajectory surface hopping (TSH),[12,24−27] are limited to relatively small systems and fast ISCs.

In contrast to NA-MD, the statistical nonadiabatic transition-state theory (NA-TST)[28−30] assumes that the "effective" transitions occur only at a minimum energy crossing point (MECP), which is the minimum on the crossing seam between the PESs of two spin states. This makes NA-TST very computationally efficient and applicable to slower ISCs in larger systems,[23,30] such as acrylates,[31] myoglobin,[32] and metal-sulfur proteins.[8,9,30,33] Another important advantage, related to a small number of electronic structure calculations required by NA-TST, is the possibility of using high-level electronic structure methods, which is critical for accurate kinetics studies.[34]

However, the difficulty of finding MECP geometry in large complex systems means that the ISC kinetics is often studied using small models. For example, the solvated metalloproteins are usually reduced to the active site models embedded in polarizable medium.[8,9,30,33] For accurate description of the ISC kinetics in large biological systems, it is important to account for the influence of the protein chains and the surrounding water molecules on the active site, which is too expensive with the conventional electronic structure methods and requires alternatives. The hybrid quantum mechanics/molecular mechanics (QM/MM) method in which a small part of the system is described with QM, while the surrounding protein chains and the solvent molecules are treated with MM, is one of such alternatives.[35−40] The main QM/MM challenge is the accurate description of the interaction between the QM and MM regions.[41] In contrast, the fragment-based fully QM methods offer a uniform quantum description of the entire

Received: June 27, 2019
Published: September 13, 2019

DOI: 10.1021/acs.jctc.9b00641
J. Chem. Theory Comput. 2019, 15, 6074−6084

system, which is a more universal and potentially more accurate approach.[42]

Fragment-based methods[43−53] provide an efficient way to predict properties of large molecular systems. The fragment molecular orbital (FMO) method,[54−58] implemented[59] in quantum chemical package GAMESS,[60,61] has been successfully used to optimize molecular geometries corresponding to minima and transition states on PES[62−65] and thus can be utilized for the conventional transition-state theory (TST) rate calculations. However, the FMO method has not been interfaced with the MECP search techniques[66] preventing its use within the NA-TST framework and hindering the studies of nonadiabatic spin-forbidden kinetics in large complex systems. An example of such systems is the electron-transferring iron−sulfur protein rubredoxin[33,67−69] that plays important role in a variety of biological processes,[70] including nitrate reduction,[71] alkane oxidation,[72] methanogenesis,[73] carbon fixation,[74] and detoxification of reactive oxygen species.[75,76] Moreover, it was shown that rubredoxin is crucial for the photosystem II activity within oxygenic organisms.[77] Rubredoxin is the smallest representative of the large class of iron−sulfur proteins participating in electron transfer by changing the oxidation state of the Fe centers. The active sites of these proteins are characterized by multiple low-lying electronic states with different spin multiplicities. The relative stability of these states is controlled by the geometry of the active site, which is sensitive to the environment. Therefore, changes in the active site environment could lead to nonadiabatic "spin-forbidden" transitions between the low-lying electronic states. The role of these transitions in biological electron transfer is not clear.

In this work, we report an implementation of a new FMO-MECP method. To test this method, we locate the MECP between the lowest energy spin states (quartet and sextet) of rubredoxin with the Fe(III) center considering the protein and solvent models of different sizes and complexities. The electronic structure methods and general MECP search method are described in Sections II and III, respectively. The implementation of FMO-MECP and its application to ISCs in rubredoxin are discussed in Section IV. In Section IV.A, FMO is applied to calculate the energy of the large rubredoxin model that includes the entire protein chain and surrounding water molecules. The scalability of the FMO gradient calculations, which is a computational bottleneck of the FMO-MECP search, is addressed. Section IV.B describes the FMO-MECP interface and its validation by comparing the MECP energies and geometries of small rubredoxin models obtained with and without the FMO fragmentation. Finally, Section IV.C demonstrates the application of a new FMO-MECP method to the full-size protein model. Concluding remarks and future outlook are presented in Section V.

II. METHODS

The detailed description of NA-TST is given in the earlier review.[30] Briefly, the microcanonical rate constant, $k(E)$, for the transition between the electronic spin states with different multiplicities is[18,28,29,78−81]

$$k(E) = \frac{N^*_{\mathrm{MECP}}(E)}{h\rho_{\mathrm{R}}(E)} \tag{1}$$

Here, h is the Planck constant, $\rho_{\mathrm{R}}(E)$ is the density of rovibrational states of the reactant, and $N^*_{\mathrm{MECP}}(E)$ is the effective number of rovibrational states at the MECP that could be written as

$$N^*_{\mathrm{MECP}}(E) = \int_0^E \rho_{\mathrm{MECP}}(E - \varepsilon_\perp) P_{\mathrm{trans}}(\varepsilon_\perp) \mathrm{d}\varepsilon_\perp \tag{2}$$

In eq 2, $\rho_{\mathrm{MECP}}(E)$ is the density of rovibrational states at the MECP, E is the total internal energy of the system, $\varepsilon_\perp$ is the component of internal energy along the reaction coordinate orthogonal to the crossing seam hypersurface, and $P_{\mathrm{trans}}(\varepsilon_\perp)$ is the transition probability at MECP. As seen from eqs 1 and 2, the MECP properties play a key role in NA-TST; thus, the calculation of the rate constant $k(E)$ requires the MECP geometry.

The MECP search[82−84] relies on the energies (E_1 and E_2) and energy gradients ($\mathbf{G}_1$ and $\mathbf{G}_2$) of the two crossing spin-diabatic states. These quantities are used to form two orthogonal gradient vectors that are perpendicular, $\mathbf{G}_\perp$, and parallel, $\mathbf{G}_\parallel$, to the seam hypersurface, as well as the effective gradient $\mathbf{G}_{\mathrm{eff}}$[30,82−88]

$$\begin{aligned} \mathbf{G}_\perp &= \mathbf{G}_1 - \mathbf{G}_2 \\ \mathbf{G}_\parallel &= \mathbf{G}_1 - \frac{\mathbf{G}_\perp}{|\mathbf{G}_\perp|}\left(\mathbf{G}_1 \cdot \frac{\mathbf{G}_\perp}{|\mathbf{G}_\perp|}\right) \\ \mathbf{G}_{\mathrm{eff}} &= \alpha(E_1 - E_2)\mathbf{G}_\perp + \mathbf{G}_\parallel \end{aligned} \tag{3}$$

The three- and two-dimensional representations of the crossing spin-diabatic potential energy surfaces (PESs) with MECP, and these gradients are shown in Figure 1. The gradient $\mathbf{G}_\perp$ points toward the seam, while the $\mathbf{G}_\parallel$ projection on the seam points toward the seam minimum. The effective gradient $\mathbf{G}_{\mathrm{eff}}$ is a linear combination of these two gradients in which $\mathbf{G}_\perp$ is weighed by the energy gap and the empirical scaling parameter α is set to 30 hartree^{-1} to achieve an optimal convergence rate to MECP geometry. The MECP geometry

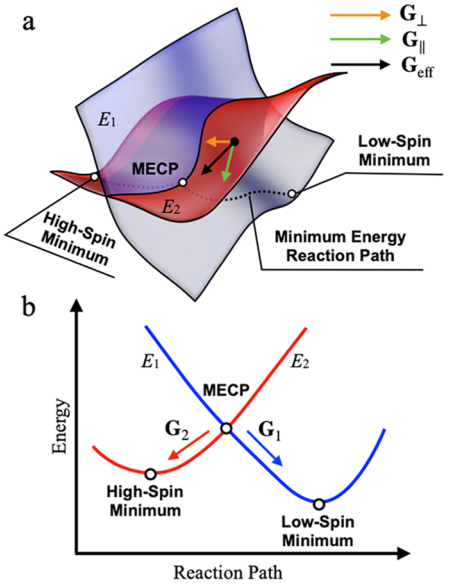

Figure 1. PES crossing of two electronic states with different spin multiplicities. (a) Three-dimensional representation showing the perpendicular, parallel, and effective gradients. (b) Two-dimensional representation of MECP along the minimum energy reaction pathway.

DOI: 10.1021/acs.jctc.9b00641
J. Chem. Theory Comput. 2019, 15, 6074−6084

search is performed by following the effective gradient using the quasi-Newton method with the Broyden−Fletcher−Goldfarb−Shanno (BFGS) Hessian update. The MECP geometry is considered to be converged when the following five parameters reach values below some predefined thresholds: the energy gap $E_1 - E_2$, max($\mathbf{G}_{\text{eff}}$), rms($\mathbf{G}_{\text{eff}}$), max($\Delta\mathbf{X}$), and rms($\Delta\mathbf{X}$). Here, $\Delta\mathbf{X} = \mathbf{X}^i - \mathbf{X}^{i-1}$ is the difference between the atomic coordinate vector $\mathbf{X}$ at the MECP search steps i and $i - 1$.

In FMO, a molecular system is divided into fragments. The electronic structure of each fragment (monomer) is calculated in the presence of the electrostatic embedding until full convergence. Then, fragment pair (dimer) calculations are performed. The total properties such as the total energy are obtained as a combination of the properties of fragments and their pairs. In this work, the frozen domain (FD) formulation of FMO is used with the dimer approximation (FDD).[62] In FD, each fragment is assigned to either the polarizable or frozen domain. Full calculations for the whole system are only done once for the initial geometry, and for each consequent step, the electronic state in the frozen domain is frozen and contributes to the embedding of the polarizable buffer and to the energy via interactions with it. Only atoms in a part of the polarizable buffer, the active domain, are optimized. In FDD, a further computational acceleration is achieved by neglecting very small contributions of pairs outside of the active domain.

III. COMPUTATIONAL DETAILS

Four models of rubredoxin protein were used (Figure 2). Models 1, 2, 3, and 4 contained 13033, 144, 68, and 973 atoms

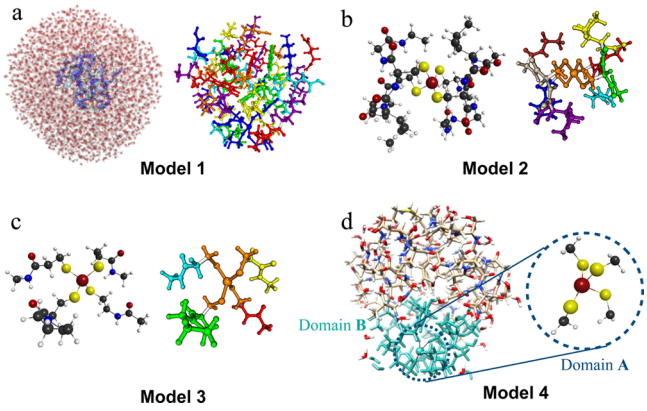

Figure 2. Four models of rubredoxin with FMO fragmentation schemes (fragments are shown with different colors). For model 1, fragmentation of water molecules is not shown. For model 4, domain **B** in FDD is in cyan, and domain **A** (**A** ⊂ **B**) is shown inside the dashed circle.

divided over 844, 9, 5, and 107 fragments, respectively. These models were based on the rubredoxin structure obtained from macromolecular neutron crystallography data (PDB 4K9F).[89] Model 1 was solvated with the Chimera software[90] using the TIP4 solvation model.[91] The smaller models 2 and 3 were made by truncating model 1. The total charge of all models was set to −1 to keep the metal center in the formal oxidation state, Fe(III). For the active site fragment, $-COO^-$ groups of aspartate and glutamate residues were protonated, while $-NH_3^+$ groups of lysine were deprotonated. We found that no DFT convergence was possible when charged residues were retained in the rubredoxin models. It has been shown earlier[92] that DFT features a small HOMO-LUMO gap for zwitterions, which is the reason why some residues had to be protonated to alleviate the problems. An improvement in the future can be obtained by a more biologically feasible protonation when DFT functionals with a better description of zwitterions become available.

We focused on the lowest energy quartet and sextet electronic states because our previous study on the isolated active site model indicated the presence of the intersection between these electronic states.[33] The large-scale energy calculations on the model 1 quartet state were performed using the FMO1 method (only fragment monomers are computed), LC-BPBE functional,[93−95] and the def2-SV(P) basis set.[96] The scalability of the FMO-MECP code was tested on model 2 using the FMO2-UHF method[97] (with dimer corrections) and 3-21G basis set.[98−100] The FMO-MECP accuracy was tested by performing the MECP search on the small model 3 using the FMO2-LC-BPBE method[101] with 6-31G basis set[102,103] and comparing the obtained MECP geometry to that of the nonfragmented model optimized with the conventional MECP method. Calculations on model 4 that contains the entire protein and crystallographic water[104] were performed using the FMO frozen domain approach with dimer approximation (FDD).[64,65] All geometry optimizations were carried out with the gradient threshold 10^{-4} hartree/bohr. In the MECP search, the following thresholds were used: $E_1 - E_2 = 10^{-5}$ hartree, max($\mathbf{G}_{\text{eff}}$) = 5×10^{-4} hartree/bohr, rms($\mathbf{G}_{\text{eff}}$) = 3×10^{-4} hartree/bohr, max($\Delta\mathbf{X}$) = 2×10^{-3} bohr, and rms($\Delta\mathbf{X}$) = 1.5×10^{-3} bohr. The scalability tests were performed on a Mira 10-petaflops IBM Blue Gene/Q supercomputer at the Argonne Leadership Computing Facility.

The initial structure of model 4 was preoptimized with the PM7 semiempirical method[104] in MOPAC.[105] The surrounding solvent in the model 4 calculations was described with the conductor-like polarizable continuum model (C-PCM).[106−108] In FMO/FDD, the active domain **A** consisted of an active site fragment; the positions of all atoms in this fragment were optimized. The polarizable domain **B** included domain **A** and other fragments within the unitless distance of 1.9 from **A**, roughly corresponding to 5 Å. The rest of the fragments were placed in domain **F**. For the lower layer (domain **F**) in the multilayer FMO, the LC-BLYP/STO-3G level of theory was used, while the higher layer (domains **A** and **B**) was treated with LC-BLYP/6-31G*. All calculations were performed using GAMESS.

Parallelization is the crucial part of large-scale calculations. The parallel calculations in GAMESS can be done using the distributed data interface (DDI) and generalized distributed data interface (GDDI). The DDI allows storage of large data arrays in the aggregate memory of distributed memory across computing nodes and provides an interface for message passing between those nodes.[109] The GDDI is built on the top of DDI and introduces a two-level hierarchical scheme. In GDDI, the parallelization is accomplished first at the upper level by assigning computational tasks to groups. Next, each group performs parallelization at the lower level by dividing its task into smaller workloads assigned to individual CPU cores.

To achieve a better parallel efficiency, FMO-MECP was also parallelized with generalized distributed data interface with three-level parallelization (GDDI/3)[110] (Figure 3). The existing two-level parallelization (GDDI/2)[109] algorithm had major technical problems, related to overwriting the fragment data of one spin state by another. Namely, in GDDI/2, there is

DOI: 10.1021/acs.jctc.9b00641
J. Chem. Theory Comput. 2019, 15, 6074−6084

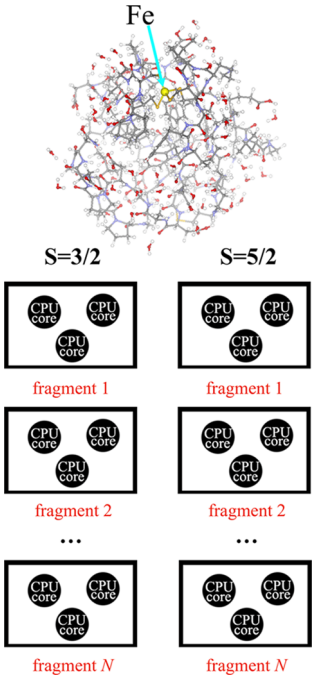

Figure 3. GDDI/3 parallelization of FMO-MECP calculations. All cores are divided into two worlds with spins $S = 3/2$ and $S = 5/2$; then, each world is divided into multiple groups, and each group consists of multiple cores. All of these calculations are done in a single GAMESS run.

a single fragment density storage (in shared memory) where the data are first stored for spin 1 and the calculation for spin 2 overwrites these data, disrupting their reuse during the MECP search. In GDDI/3, all CPU cores are divided into two worlds, and each spin state is calculated by one world. Each world keeps its own set of electron densities for the spin state it calculates, and convergence is significantly improved. Furthermore, each world uses a two-level parallelization (all CPU cores in the world are divided into groups; one group calculates a fragment or a dimer by dividing work between cores in the group). To divide work between groups in GDDI/3, a dynamic load balancing was developed solving the conflict between the load balancing counters in different worlds by implementing a new request mechanism for data servers.

Transition-metal complexes often have low-lying excited states. In the Fe(III)-containing protein rubredoxin used to validate the FMO-MECP implementation, an excited quartet state lying about 10 kcal/mol above the ground quartet was causing the MECP search algorithm to switch between these two states hindering convergence. In FMO calculations, molecular orbitals (MOs) of fragments are stored and reused for subsequent geometries. However, dimer MOs are not reused; instead, the initial density for the dimer *IJ* is constructed as a block-wise addition of monomer *I* and *J* densities. Therefore, there is no guarantee that the electron state of dimers is the same in consequent geometries.

To facilitate the continuation of the same state surface, in this work, a new option to store dimer densities in the DDI memory was implemented, similar to the storage of monomer densities, but accomplished in a different DDI array. Only the densities of SCF dimers are stored (most dimers are treated with the electrostatic approximation[111] for which dimer densities are not needed). It was found that this option is critical for finding MECP in the case of a system with multiple low-lying states. It should be noted that even with reading orbitals from the previous geometry, there is no guarantee that SCF would not converge to a different state; however, with such orbitals, convergence to the desired state is much more likely. In addition to the prevention of surface flipping, there is also some speed-up achieved by using better initial orbitals.

IV. RESULTS AND DISCUSSION

IV.A. Parallel Scalability Tests. To test the scalability of the FMO method applied to rubredoxin, single-point energy FMO1 calculations were performed. In the one-body FMO1 approximation, the interaction between a fragment and the rest of the system is described by the electrostatic field constructed from the electronic densities of surrounding fragments. Potentially, the interaction between fragments could be treated more accurately with the two-body approximation (FMO2) in which the interaction energies within the pairs of fragments are calculated directly by subtraction of (FMO1) energies of individual fragments from energies of the fragment pairs. However, for the scalability tests, the FMO1 approximation is adequate. The tests were carried out on the large model of solvated rubredoxin (model 1), which includes 796 atoms of the entire protein and 4079 water molecules. The model is partitioned into 844 fragments, including 28 fragments that represent protein, 815 fragments each consisting of five water molecules, and one fragment containing four water molecules. The fragment with four water molecules is the result of the fact that the total number of water molecules in the model is not a multiple of five. The active site fragment has the total charge of −1 and contains the Fe(III) metal center surrounded by four cysteine residues. The protein chain is fragmented in such a way that each fragment contains two amino acids.

All single-point energy calculations were performed for the quartet spin state using 4096, 8192, 16,384, 32,768, 65,536, and 131,072 CPU cores distributed between 128 dynamically load balanced groups in GDDI. The dynamic load balancing scheme attempts to spread out possibly unequal work assignments based on the rate at which different nodes complete their tasks, which, in the case of fragments with a similar number of basis functions, usually produces a reasonable distribution of fragment calculations across CPUs.[109] As seen from Figure 4a, the energy calculation scales well up to 16,384 CPU cores. These results are promising and could be further improved by using the heuristic static load balancing algorithm, as was previously demonstrated in the FMO calculations on ubiquitin.[112]

To test the scalability of the FMO2 energy gradient, which is the computational bottleneck of the MECP geometry optimization, calculations were performed on the quartet state of model 2 comprised of 144 atoms and nine fragments. The active site fragment contains the Fe(III) center surrounded by four $-SCH_2-$ groups. Other eight fragments contain the residues nearest to the metal center. The calculations were carried out on 128, 256, 512, 1024, and 2048 CPU cores with dynamic load balancing scheme between eight CPU groups. Figure 4b shows that the single energy gradient computational time decreases almost linearly with a number of CPU cores, meaning that the parallel efficiency of this calculation using our code is high.

IV.B. Validation of FMO-MECP Method. To validate the newly developed FMO-MECP method against the conventional nonfragment method, the MECP geometry search for quartet/sextet intersection was performed on small model 3

DOI: 10.1021/acs.jctc.9b00641
J. Chem. Theory Comput. 2019, 15, 6074−6084

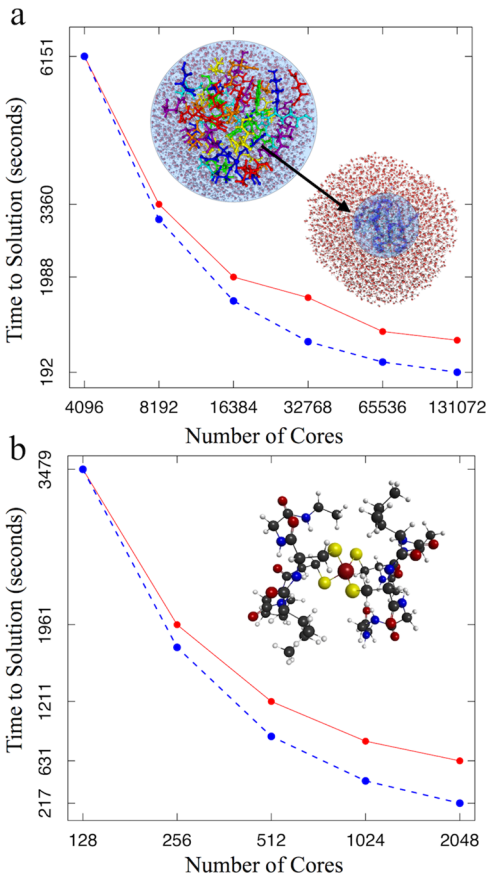

Figure 4. Scaling of FMO GDDI/2 calculations as a function of the number of CPU cores. (a) Time to complete an FMO1 energy calculation on model 1 (active site and solvation shell are shown in the inset). (b) Time to complete an FMO2 energy gradient calculation on model 2 (shown in the inset). The red solid and blue dashed lines depict measured and ideal timings, respectively.

with the FMO2-DFT (DFT = LC-BPBE/6-31G) levels of theory. The root mean square deviation between the MECP geometries found with the FMO-based and conventional methods is only 0.0479 Å, indicating an excellent agreement between the two structures (Figure 5a). To compare the relative energies obtained with the FMO-based and conventional MECP methods, the FMO equilibrium geometry optimizations were also performed for the quartet and sextet states. The differences between the relative DFT and FMO-DFT energies do not exceed 0.85 kcal/mol (Figure 5b). It is important to notice that according to these calculations, the MECP and quartet minimum structures are very similar, while their energies are nearly degenerate. That is not the case for the previously studied small active site model.[33] Thus, the size of the protein model can affect the MECP geometry and using large models in the ISC kinetics studies can be important.

It was demonstrated previously that the transitions between electronic spin states of rubredoxin are mediated by changes of the active site torsion angles α, β, and γ (Figure 6).[33] The maximum difference between the values of these torsion angles obtained with the conventional MECP and FMO-MECP methods is only 0.31 degrees (Table 1). Thus, the new FMO-MECP method can accurately predict the energies and geometries needed for the ISC kinetics calculations.

IV.C. Application of FMO-MECP to Full-Size Protein Model. To demonstrate the capability of the new method, the

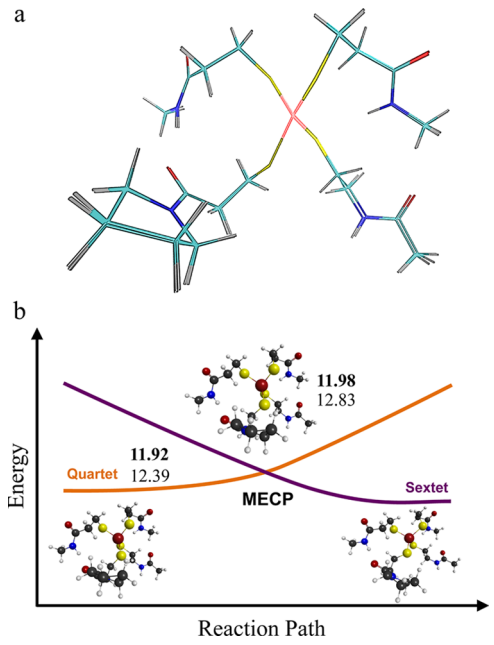

Figure 5. Comparison between the MECP geometries of model 3 found with the conventional nonfragment and new FMO-MECP methods. (a) Overlapping MECP geometries obtained with the two methods. (b) Energies (kcal/mol) of the MECP and quartet minimum with respect to the sextet minimum. The bold (upper) and regular (lower) values are obtained with the FMO-based and conventional methods, respectively.

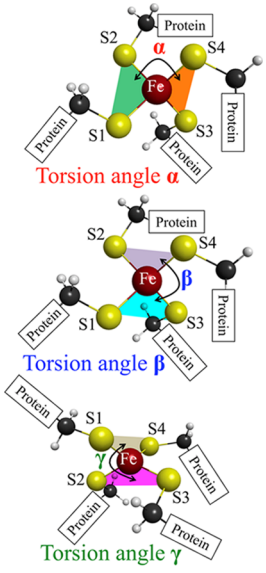

Figure 6. Torsion angles of the rubredoxin active site.

Table 1. Active Site Torsion Angles (Degrees) Obtained with the FMO-MECP and Convectional MECP Methods[a]

method	angle α	angle β	angle γ
FMO-MECP	92.46	62.21	64.41
MECP	92.59	61.90	64.20

[a]Calculations were performed at the LC-BPBE/6-31G level of theory.

FMO-MECP search was performed on the entire rubredoxin and crystallographic water, while the surrounding solvent was simulated via PCM (model 4). This model contained 973

DOI: 10.1021/acs.jctc.9b00641
J. Chem. Theory Comput. 2019, 15, 6074−6084

atoms divided into 107 FMO fragments. Protein fragments contained one protein residue per fragment, and each explicit water molecule was used as a single fragment. The calculations were carried out using the FMO/FDD method optimizing the geometry of the active site (domain **A**), while the surrounding atoms in domains **B** and **F** were constrained (Figure 2d).

To determine the effect of the model size on the optimized MECP geometry, the values of torsion angles α, β, and γ in the active site fragments are compared for models 3 and 4 (Table 2). The significant differences of 6.96, 13.02, and 15.05 degrees

Table 2. Comparison of Fe(III) Rubredoxin Active Site Torsion Angles at the Quartet/Sextet MECP in Models 3 and 4[a]

model	angle α	angle β	angle γ
3	92.46	62.21	64.41
4	85.50	75.23	79.46

[a]Values of torsion angles are obtained with the FMO2 method at the LC-BPBE/6-31G level of theory.

clearly demonstrate the importance of including the protein environment around the active site in the computational model.

To reveal insights into the nature of the stability of the two spin states, the total FMO energy for spin state S is decomposed into the internal monomer $E_I'^S$ and pair interaction energies (PIE) ΔE_{IJ}^S (both include solvent contributions).

$$E^S = \sum_{I=1}^{N} E_I'^S + \sum_{I>J}^{N} \Delta E_{IJ}^S \tag{4}$$

At MECP, the energies of the quartet and sextet states are the same, $E^4 = E^6$. However, the components differ.

$$\Delta E = E^4 - E^6 = \sum_{I=1}^{N} \Delta E_I' + \sum_{I>J}^{N} \Delta\Delta E_{IJ} \tag{5}$$

where

$$\Delta E_I' = E_I'^4 - E_I'^6$$
$$\Delta\Delta E_{IJ} = \Delta E_{IJ}{}^4 - \Delta E_{IJ}{}^6 \tag{6}$$

The results are analyzed for the model 4 using the FMO/FDD method with the Fe-site (fragment $J = 6$) included in the active domain **A**. In this case, the energies are written as

$$\Delta E = E^4 - E^6 = \sum_{I\in\mathbf{B}} \Delta E_I' + \sum_{I\in\mathbf{B}} \Delta\Delta E_{I,6} + \sum_{I\in\mathbf{F}} \Delta\Delta E_{I,6} \tag{7}$$

The fragments of model 4 with large absolute values of $\Delta E_I'$ and $\Delta\Delta E_{I,6}$ are depicted in Figure 7.

The numerical values obtained from the PIE analysis are summarized in Table 3. Overall, monomers in the sextet state are more stable (by about 55 kcal/mol). In the quartet state, this difference is compensated by the pair interactions so that the total energies of the quartet and sextet are the same. It can be seen that the quartet state of the Fe-site fragment is less stable than the sextet by 23.3 kcal/mol. The adjacent XAA-8 fragment is also less stable by 35.4 kcal/mol. However, pair interactions make up for these two major differences in monomer energies: there is a large contribution due to the

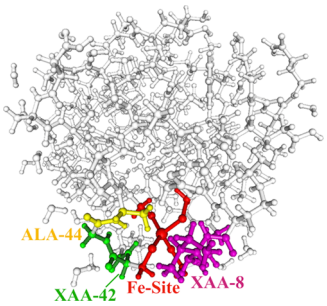

Figure 7. Fragments making significant contributions to the energy differences between quartet and sextet electronic spin states. The depicted geometry corresponds to the optimized FMO-MECP structure of model 4.

interaction of the Fe-site and XAA-8 and XAA-42. All other contributions are 4 kcal/mol or less (the largest is due to ALA-44). Explicit water molecules contribute less than 1 kcal/mol (they may still be important for determining the structure). The choice of the frozen domain was appropriate as it contributes little to the stabilization energy components and is sufficiently separated from the active site. The stability analysis of spin states described here may be used for designing specific protein mutations aimed at changing the MECP structures and controlling the spin-dependent processes in biological systems.

The spin density at the minimum energy crossing is shown in Figure 8. For the sextet, five unpaired α electrons determine that only α-dominated spin density is seen. The quartet state (three unpaired electrons) features competition between α and β electrons, and the latter are also relevant for the spin density. In addition, the spin density for the sextet is very much localized on the iron-containing fragment. The quartet, however, has a β-density leaking to XAA-8, which is consistent with its large energetic contribution in Table 3.

V. CONCLUSIONS

To facilitate the studies of the intersystem crossing kinetics in large complex systems, we developed and implemented a new fragment molecular orbital method capable of finding MECP between two electronic states with different spin multiplicities. We also introduced several improvements to the FMO method necessary for the computationally efficient MECP search, including preventing switches between low-lying electronic states by storing dimer densities in shared memory. Energy calculations on the 13033-atom model of the protein rubredoxin solvated with water show a very good scaling up to 65,536 CPU cores and a reasonable scaling up to 131,072 cores at the FMO1-DFT level of theory.[113] The new FMO-MECP method was validated on a small rubredoxin model by comparing the results obtained with the new and conventional nonfragmented MECP geometry optimizations. The difference between the FMO and nonfragmented relative energies of the quartet/sextet MECP (0.85 kcal/mol) is within chemical accuracy. The MECP geometries are also in excellent agreement with each other (RMSD = 0.0479 Å). At the MECP geometry, the thiolate torsion angles in the active site of rubredoxin[33] obtained with the FMO and nonfragmented calculations agree within 0.31°.

We applied the new FMO-MECP method to a large model of the protein rubredoxin with crystallographic water molecules treated by FMO and the rest of the solvent described by the polarization continuum model. While the

DOI: 10.1021/acs.jctc.9b00641
J. Chem. Theory Comput. 2019, 15, 6074−6084

Table 3. Contributions of Fragments to the Stability (Energies in kcal/mol) of Quartet and Sextet Spin States[a]

I	fragment name	composition[b] as in PDB	separation $R_{I,6}$	domain	monomer $\Delta E'_I$	dimer $\Delta\Delta E_{I,6}$
4	VAL-5	Val-4	1.28	B	0.2	0.0
5	XAA-6	Cys-5, Lys-6	0.00	B	0.6	2.0
6	Fe-site	Fe, Cys-5, Cys-8, Cys-38, Cys-41	0.00	A	23.3	0.0
7	XAA-8	Ile-7, Cys-8	0.80	B	35.4	−41.4
8	TYR-11	Tyr-10	1.06	B	0.0	2.3
9	ILE-12	Ile-11	1.42	B	0.3	−0.1
34	TRP-37	Trp-36	1.27	B	−0.1	0.3
35	VAL-38	Val-37	0.00	B	0.1	−0.1
36	XAA-39	Pro-39	0.92	B	−0.5	−2.2
37	ILE-41	Ile-40	0.00	B	−1.1	−0.8
38	XAA-42	Gly-42, Cys-41	0.85	B	−2.8	−10.4
39	ALA-44	Ala-43, Gly-42	1.32	B	1.6	−4.1
40	PRO-45	Pro-44	1.55	B	−1.3	−0.6
43	GLU-48	Glu-47	0.93	B	0.4	−0.4
44	PHE-49	Phe-48	1.38	B	−0.3	−1.0
45	GLU-50	Glu-49	1.55	B	0.1	0.3
54	HOH6	1 water	1.51	B	0.0	−0.2
57	HOH9	1 water	1.41	B	−0.1	−0.2
62	HOH14	1 water	1.50	B	0.0	0.6
74	HOH26	1 water	1.48	B	0.0	−0.8
76	HOH28	1 water	1.63	B	0.0	0.9
77	HOH29	1 water	1.43	B	0.1	−0.2
86	HOH38	1 water	1.28	B	0.0	0.5
	others[c]	composite	>1.99	F	0.0	0.2
	total[d]				55.9	−55.4

[a]The separation is unitless (the geometrical distance between two atoms divided by the sum of their van der Waals radii; for O−H pairs, $R = 1$ corresponds to 2.6 Å). Negative values of $\Delta E'_I$ and $\Delta\Delta E_{I,6}$ mean that the quartet is more stable than the sextet. [b]Fragment residues in PDB are denoted by the first capital letter (Cys-5, etc.), whereas fragments are denoted by capital letters (VAL-5, etc.). Note that the residue numbering in the PDB file starts from 0 so that Glu-49 is the 50th residue in the PDB entry 4K9F, and so in FMO, it corresponds to GLU-50 (numbering from 1). [c]The value given here is $\sum_{I\in \mathbf{F}} \Delta\Delta E_{I,6}$. [d]The sum of the values in the $\Delta E'_I$ and $\Delta\Delta E_{I,6}$ columns should be zero at the perfect energy crossing; the small deviation (0.5 kcal/mol) is due to round off errors (the exact energy difference computed from the total energies is 0.001 kcal/mol).

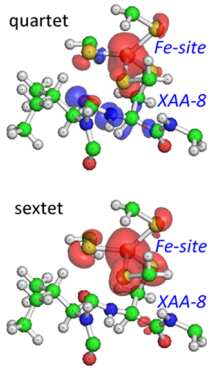

Figure 8. Spin density distribution in model 4. Only Fe-site and XAA-8 fragments are shown, where the spin density is nonzero. The red and blue surfaces show positive (α-dominated) and negative (β-dominated) values of the spin density, respectively.

optimized MECP between the lowest quartet and sextet spin states has similar geometry to that in the small active site model, there are significant differences in the coordination of the thiolate ligands to the Fe(III) centers. This indicates that the use of large protein models with explicit solvent can be important for describing kinetics of spin-forbidden transitions in the metal-containing active sites and, therefore, for understanding how metalloproteins function in realistic biological environments. We also show how the FMO energy decomposition can be used to determine which part of the protein is responsible for stabilization of each spin states. We speculate that such analysis could be useful for designing protein mutations aimed at changing the MECP structures and controlling the spin-dependent processes in metalloproteins, including catalysis and electron transfer.

It is important to note that in NA-TST, energies are evaluated for specific structures located on the multidimensional PESs and do not include the effect of temperature or conformational sampling. In future, by extending the techniques developed to evaluate the free binding energy in the framework of MM and QM/MM methods, it should be possible to take advantage of the recent progress in the FMO/MD methodology capable of MD simulations on the nanosecond time scale.[114] In addition, MD and Monte Carlo techniques could be useful in locating the global minimum energy crossing.

■ ASSOCIATED CONTENT

Supporting Information

The Supporting Information is available free of charge on the ACS Publications website at DOI: 10.1021/acs.jctc.9b00641.

Atomic Cartesian coordinates of the MECP, quartet, and sextet geometries for all models and fragmentation details for model 4 (ZIP)

■ AUTHOR INFORMATION

Corresponding Author

*E-mail: svarganov@unr.edu. Phone: +1 775-784-1406.

DOI: 10.1021/acs.jctc.9b00641
J. Chem. Theory Comput. 2019, 15, 6074−6084

ORCID

Dmitri G. Fedorov: 0000-0003-2530-5989

Sergey A. Varganov: 0000-0001-8301-3891

Present Address

[‖]Department of Chemistry, Purdue University, 560 Oval Drive, West Lafayette, Indiana, 47906, United States.

Notes

The authors declare no competing financial interest.

■ ACKNOWLEDGMENTS

The financial support was provided by the National Science Foundation through a CAREER award (CHE-1654547) to S.A.V. Supercomputer time was provided through the Department of Energy (DOE) ASCR Leadership Computing Challenge (ALCC) award. This research used resources of the Argonne Leadership Computing Facility, which is a DOE Office of Science User Facility supported under Contract DE-AC02-06CH11357. Y.A. and D.S.K. were supported by the DOE Office of Science.

■ REFERENCES

(1) Jasper, A. W.; Dawes, R. Non-Born-Oppenheimer Molecular Dynamics of the Spin-Forbidden Reaction $O(^3P) + CO(X^1\Sigma^+) \rightarrow CO_2\ (\tilde{X}^1\Sigma_g^+)$. *J. Chem. Phys.* **2013**, *139*, 154313.

(2) Balucani, N.; Leonori, F.; Casavecchia, P.; Fu, B.; Bowman, J. M. Crossed Molecular Beams and Quasiclassical Trajectory Surface Hopping Studies of the Multichannel Nonadiabatic $O(^3P)$ + Ethylene Reaction at High Collision Energy. *J. Phys. Chem. A* **2015**, *119*, 12498−12511.

(3) Maeda, S.; Taketsugu, T.; Ohno, K.; Morokuma, K. From Roaming Atoms to Hopping Surfaces: Mapping Out Global Reaction Routes in Photochemistry. *J. Am. Chem. Soc.* **2015**, *137*, 3433−3445.

(4) Ahmadvand, S.; Zaari, R. R.; Varganov, S. A. Spin-Forbidden and Spin-Allowed Cyclopropenone ($c\text{-}H_2C_3O$) Formation in Interstellar Medium. *Astrophys. J.* **2014**, *795*, 173.

(5) Goodrow, A.; Bell, A. T.; Head-Gordon, M. Are Spin-Forbidden Crossings a Bottleneck in Methanol Oxidation? *J. Phys. Chem. C* **2009**, *113*, 19361−19364.

(6) Strickland, N.; Harvey, J. N. Spin-Forbidden Ligand Binding to the Ferrous−Heme Group: Ab Initio and DFT Studies. *J. Phys. Chem. B* **2007**, *111*, 841−852.

(7) Alcantara, R. E.; Xu, C.; Spiro, T. G.; Guallar, V. A Quantum-Chemical Picture of Hemoglobin Affinity. *Proc. Natl. Acad. Sci.* **2007**, *104*, 18451−18455.

(8) Yson, R. L.; Gilgor, J. L.; Guberman, B. A.; Varganov, S. A. Protein Induced Singlet−Triplet Quasidegeneracy in the Active Site of [NiFe]-Hydrogenase. *Chem. Phys. Lett.* **2013**, *577*, 138−141.

(9) Kaliakin, D. S.; Zaari, R. R.; Varganov, S. A. Effect of H_2 Binding on the Nonadiabatic Transition Probability between Singlet and Triplet States of the [NiFe]-Hydrogenase Active Site. *J. Phys. Chem. A* **2015**, *119*, 1066−1073.

(10) Frutos, L. M.; Andruniów, T.; Santoro, F.; Ferré, N.; Olivucci, M. Tracking the Excited-State Time Evolution of the Visual Pigment with Multiconfigurational Quantum Chemistry. *Proc. Natl. Acad. Sci.* **2007**, *104*, 7764−7769.

(11) Schoenlein, R.; Peteanu, L.; Mathies, R.; Shank, C. The First Step in Vision : Femtosecond Isomerization of Rhodopsin. *Science* **1991**, *254*, 412−415.

(12) Mai, S.; Marquetand, P.; González, L. A General Method to Describe Intersystem Crossing Dynamics in Trajectory Surface Hopping. *Int. J. Quantum Chem.* **2015**, *115*, 1215−1231.

(13) Crespo-Hernández, C. E.; Cohen, B.; Hare, P. M.; Kohler, B. Ultrafast Excited-State Dynamics in Nucleic Acids. *Chem. Rev.* **2004**, *104*, 1977−2020.

(14) Weinkauf, R.; Schermann, J. P.; De Vries, M. S.; Kleinermanns, K. Molecular Physics of Building Blocks of Life under Isolated or Defined Conditions. *Eur. Phys. J. D.* **2002**, *20*, 309−316.

(15) Stephansen, A. B.; Brogaard, R. Y.; Kuhlman, T. S.; Klein, L. B.; Christensen, J. B.; Sølling, T. I. Surprising Intrinsic Photostability of the Disulfide Bridge Common in Proteins. *J. Am. Chem. Soc.* **2012**, *134*, 20279−20281.

(16) de Vries, M. S.; Hobza, P. Gas-Phase Spectroscopy of Biomolecular Building Blocks. *Annu. Rev. Phys. Chem.* **2007**, *58*, 585−612.

(17) Perot, M.; Lucas, B.; Barat, M.; Fayeton, J. A.; Jouvet, C. Mechanisms of UV Photodissociation of Small Protonated Peptides. *J. Phys. Chem. A* **2010**, *114*, 3147−3156.

(18) Harvey, J. N. Spin-Forbidden Reactions: Computational Insight into Mechanisms and Kinetics. *Wiley Interdiscip. Rev.: Comput. Mol. Sci.* **2014**, *4*, 1−14.

(19) Marian, C. M. Spin-Orbit Coupling and Intersystem Crossing in Molecules. *Wiley Interdiscip. Rev.: Comput. Mol. Sci.* **2012**, *2*, 187−203.

(20) Fedorov, D. A.; Lykhin, A. O.; Varganov, S. A. Predicting Intersystem Crossing Rates with AIMS-DFT Molecular Dynamics. *J. Phys. Chem. A* **2018**, *122*, 3480−3488.

(21) Fedorov, D. A.; Pruitt, S. R.; Keipert, K.; Gordon, M. S.; Varganov, S. A. Ab Initio Multiple Spawning Method for Intersystem Crossing Dynamics: Spin-Forbidden Transitions between3B1and1A1States of GeH_2. *J. Phys. Chem. A* **2016**, *120*, 2911−2919.

(22) Curchod, B. F.; Rauer, C.; Marquetand, P.; González, L.; Martínez, T. J. Communication: GAIMS—Generalized Ab Initio Multiple Spawning for Both Internal Conversion and Intersystem Crossing Processes. *J. Chem. Phys.* **2016**, *144*, 101102.

(23) Jasper, A. W. Multidimensional Effects in Nonadiabatic Statistical Theories of Spin-Forbidden Kinetics: A Case Study of $^3O + CO \rightarrow CO_2$. *J. Phys. Chem. A* **2015**, *119*, 7339−7351.

(24) Zaari, R. R.; Varganov, S. A. Nonadiabatic Transition State Theory and Trajectory Surface Hopping Dynamics: Intersystem Crossing Between $^3B_1$ and $^1A_1$ States of SiH_2. *J. Phys. Chem. A* **2015**, *119*, 1332−1338.

(25) Atkins, A. J.; González, L. Trajectory Surface-Hopping Dynamics Including Intersystem Crossing in $[Ru(Bpy)_3]^{2+}$. *J. Phys. Chem. Lett.* **2017**, *8*, 3840−3845.

(26) Plasser, F.; Gómez, S.; Menger, M. F.; Mai, S.; González, L. Highly Efficient Surface Hopping Dynamics Using a Linear Vibronic Coupling Model. *Phys. Chem. Chem. Phys.* **2018**, *21*, 57−69.

(27) Duan, J.-X.; Zhou, Y.; Xie, Z.-Z.; Sun, T.-L.; Cao, J. Incorporating Spin−Orbit Effects into Surface Hopping Dynamics Using the Diagonal Representation: A Linear-Response Time-Dependent Density Functional Theory Implementation with Applications to 2-Thiouracil. *Phys. Chem. Chem. Phys.* **2018**, *20*, 15445−15454.

(28) Lorquet, J. C.; Leyh-Nihant, B. Nonadiabatic Unimolecular Reactions. 1. A Statistical Formulation for the Rate Constants. *J. Phys. Chem.* **1988**, *92*, 4778−4783.

(29) Harvey, J. N.; Aschi, M. Spin-Forbidden Dehydrogenation of Methoxy Cation: A Statistical View. *Phys. Chem. Chem. Phys.* **1999**, *1*, 5555−5563.

(30) Lykhin, A. O.; Kaliakin, D. S.; dePolo, G. E.; Kuzubov, A. A.; Varganov, S. A. Nonadiabatic Transition State Theory: Application to Intersystem Crossings in the Active Sites of Metal-sulfur Proteins. *Int. J. Quantum Chem.* **2016**, *116*, 750−761.

(31) Liu, S.; Srinivasan, S.; Tao, J.; Grady, M. C.; Soroush, M.; Rappe, A. M. Modeling Spin-Forbidden Monomer Self-Initiation Reactions in Spontaneous Free-Radical Polymerization of Acrylates and Methacrylates. *J. Phys. Chem. A* **2014**, *118*, 9310−9318.

(32) Harvey, J. N. Understanding the Kinetics of Spin-Forbidden Chemical Reactions. *Phys. Chem. Chem. Phys.* **2007**, *9*, 331−343.

(33) dePolo, G. E.; Kaliakin, D. S.; Varganov, S. A. Spin-Forbidden Transitions between Electronic States in the Active Site of Rubredoxin. *J. Phys. Chem. A* **2016**, *120*, 8691−8698.

DOI: 10.1021/acs.jctc.9b00641
J. Chem. Theory Comput. 2019, 15, 6074−6084

(34) Pokhilko, P.; Shannon, R.; Glowacki, D.; Wang, H.; Krylov, A. I. Spin-Forbidden Channels in Reactions of Unsaturated Hydrocarbons with $O(^3P)$. *J. Phys. Chem. A* **2018**, *123*, 482−491.
(35) Askerka, M.; Ho, J.; Batista, E. R.; Gascón, J. A.; Batista, V. S. *Methods Enzymol.* **2016**, *577*, 443−481.
(36) Marín, M. D. C.; De Vico, L.; Dong, S. S.; Gagliardi, L.; Truhlar, D. G.; Olivucci, M. Assessment of MC-PDFT Excitation Energies for a Set of QM/MM Models of Rhodopsins. *J. Chem. Theory Comput.* **2019**, *15*, 1915−1923.
(37) Duster, A. W.; Garza, C. M.; Aydintug, B. O.; Negussie, M. B.; Lin, H. Adaptive Partitioning QM/MM for Molecular Dynamics Simulations: 6. Proton Transport through a Biological Channel. *J. Chem. Theory Comput.* **2018**, *15*, 892−905.
(38) Dziedzic, J.; Head-Gordon, T.; Head-Gordon, M.; Skylaris, C.-K. Mutually Polarizable QM/MM Model with in Situ Optimized Localized Basis Functions. *J. Chem. Phys.* **2019**, *150*, No. 074103.
(39) Ganguly, A.; Boulanger, E.; Thiel, W. Importance of MM Polarization in QM/MM Studies of Enzymatic Reactions: Assessment of the QM/MM Drude Oscillator Model. *J. Chem. Theory Comput.* **2017**, *13*, 2954−2961.
(40) Nechay, M. R.; Valdez, C. E.; Alexandrova, A. N. Computational Treatment of Metalloproteins. *J. Phys. Chem. B* **2015**, *119*, 5945−5956.
(41) Duarte, F.; Amrein, B. A.; Blaha-Nelson, D.; Kamerlin, S. C. Recent Advances in QM/MM Free Energy Calculations Using Reference Potentials. *Biochim. Biophys. Acta, Gen. Subj.* **2015**, *1850*, 954−965.
(42) Gordon, M. S.; Fedorov, D. G.; Pruitt, S. R.; Slipchenko, L. V. Fragmentation Methods: A Route to Accurate Calculations on Large Systems. *Chem. Rev.* **2011**, *112*, 632−672.
(43) Otto, P.; Ladik, J. Investigation of the Interaction between Molecules at Medium Distances I. SCF LCAO MO Supermolecule, Perturbational and Mutually Consistent Calculations for Two Interacting HF and CH_2O Molecules. *Chem. Phys.* **1975**, *8*, 192−200.
(44) Gao, J. Toward a Molecular Orbital Derived Empirical Potential for Liquid Simulations. *J. Phys. Chem. B* **1997**, *101*, 657−663.
(45) Fang, T.; Li, Y.; Li, S. Generalized Energy-based Fragmentation Approach for Modeling Condensed Phase Systems. *Wiley Interdiscip. Rev.: Comput. Mol. Sci.* **2017**, *7*, No. e1297.
(46) Liu, J.; Zhang, J. Z.; He, X. Fragment Quantum Chemical Approach to Geometry Optimization and Vibrational Spectrum Calculation of Proteins. *Phys. Chem. Chem. Phys.* **2016**, *18*, 1864−1875.
(47) Kobayashi, R.; Amos, R.; Collins, M. A. Microsolvation within the Systematic Molecular Fragmentation by Annihilation Approach. *J. Phys. Chem. A* **2016**, *121*, 334−341.
(48) Friedrich, J.; Yu, H.; Leverentz, H. R.; Bai, P.; Siepmann, J. I.; Truhlar, D. G. Water 26-Mers Drawn from Bulk Simulations: Benchmark Binding Energies for Unprecedentedly Large Water Clusters and Assessment of the Electrostatically Embedded Three-Body and Pairwise Additive Approximations. *J. Phys. Chem. Lett.* **2014**, *5*, 666−670.
(49) Sahu, N.; Gadre, S. R. Vibrational Infrared and Raman Spectra of Polypeptides: Fragments-in-Fragments within Molecular Tailoring Approach. *J. Chem. Phys.* **2016**, *144*, 114113.
(50) Gao, J.; Truhlar, D. G.; Wang, Y.; Mazack, M. J.; Löffler, P.; Provorse, M. R.; Rehak, P. Explicit Polarization: A Quantum Mechanical Framework for Developing Next Generation Force Fields. *Acc. Chem. Res.* **2014**, *47*, 2837−2845.
(51) Jose, K. J.; Raghavachari, K. Evaluation of Energy Gradients and Infrared Vibrational Spectra through Molecules-in-Molecules Fragment-Based Approach. *J. Chem. Theory Comput.* **2015**, *11*, 950−961.
(52) Liu, J.; Herbert, J. M. Pair−Pair Approximation to the Generalized Many-Body Expansion: An Alternative to the Four-Body Expansion for Ab Initio Prediction of Protein Energetics via Molecular Fragmentation. *J. Chem. Theory Comput.* **2016**, *12*, 572−584.
(53) Nishizawa, H.; Nishimura, Y.; Kobayashi, M.; Irle, S.; Nakai, H. Three Pillars for Achieving Quantum Mechanical Molecular Dynamics Simulations of Huge Systems: Divide-and-conquer, Density-functional Tight-binding, and Massively Parallel Computation. *J. Comput. Chem.* **2016**, *37*, 1983−1992.
(54) Kitaura, K.; Ikeo, E.; Asada, T.; Nakano, T.; Uebayasi, M. Fragment Molecular Orbital Method: An Approximate Computational Method for Large Molecules. *Chem. Phys. Lett.* **1999**, *313*, 701−706.
(55) Fedorov, D. G.; Kitaura, K. Extending the Power of Quantum Chemistry to Large Systems with the Fragment Molecular Orbital Method. *J. Phys. Chem. A* **2007**, *111*, 6904−6914.
(56) Fedorov, D. G.; Nagata, T.; Kitaura, K. Exploring Chemistry with the Fragment Molecular Orbital Method. *Phys. Chem. Chem. Phys.* **2012**, *14*, 7562−7577.
(57) Tanaka, S.; Mochizuki, Y.; Komeiji, Y.; Okiyama, Y.; Fukuzawa, K. Electron-Correlated Fragment-Molecular-Orbital Calculations for Biomolecular and Nano Systems. *Phys. Chem. Chem. Phys.* **2014**, *16*, 10310−10344.
(58) Fedorov, D. G. The Fragment Molecular Orbital Method: Theoretical Development, Implementation in GAMESS, and Applications. *Wiley Interdiscip. Rev. Comput. Mol. Sci.* **2017**, *7*, No. e1322.
(59) Fedorov, D. G.; Kitaura, K. The Importance of Three-Body Terms in the Fragment Molecular Orbital Method. *J. Chem. Phys.* **2004**, *120*, 6832−6840.
(60) Schmidt, M. W.; Baldridge, K. K.; Boatz, J. A.; Elbert, S. T.; Gordon, M. S.; Jensen, J. H.; Koseki, S.; Matsunaga, N.; Nguyen, K. A.; Su, S.; Windus, T. L. General Atomic and Molecular Electronic Structure System. *J. Comput. Chem.* **1993**, *14*, 1347−1363.
(61) Gordon, M. S.; Schmidt, M. W. Advances in Electronic Structure Theory: GAMESS a Decade Later. In *Theory and Applications of Computational Chemistry*; Dykstra, C. E.; Frenking, G.; Kim, K. S.; Scuseria, G. E., Eds.; Elsevier: Amsterdam, 2005; pp. 1167−1189.
(62) Fedorov, D. G.; Ishida, T.; Uebayasi, M.; Kitaura, K. The Fragment Molecular Orbital Method for Geometry Optimizations of Polypeptides and Proteins. *J. Phys. Chem. A* **2007**, *111*, 2722−2732.
(63) Fedorov, D. G.; Alexeev, Y.; Kitaura, K. Geometry Optimization of the Active Site of a Large System with the Fragment Molecular Orbital Method. *J. Phys. Chem. Lett.* **2011**, *2*, 282−288.
(64) Nakata, H.; Fedorov, D. G.; Nagata, T.; Kitaura, K.; Nakamura, S. Simulations of Chemical Reactions with the Frozen Domain Formulation of the Fragment Molecular Orbital Method. *J. Chem. Theory Comput.* **2015**, *11*, 3053−3064.
(65) Nakata, H.; Fedorov, D. G. Efficient Geometry Optimization of Large Molecular Systems in Solution Using the Fragment Molecular Orbital Method. *J. Phys. Chem. A* **2016**, *120*, 9794−9804.
(66) Matsunaga, N.; Koseki, S. Modeling of Spin-Forbidden Reactions. In *Reviews in Computational Chemistry*, Lipkowitz, K. B.; Larter, R.; Cundari, T. R. (Eds), Wiley, Hoboken, 2004, Vol. *20*, pp. 101−152.
(67) Kennepohl, P.; Solomon, E. I. Electronic Structure Contributions to Electron-Transfer Reactivity in Iron−Sulfur Active Sites: 3. Kinetics of Electron Transfer. *Inorg. Chem.* **2003**, *42*, 696−708.
(68) Zanello, P. The Competition between Chemistry and Biology in Assembling Iron−Sulfur Derivatives. Molecular Structures and Electrochemistry. Part II. $\{[Fe_2S_2](S\gamma Cys)_4\}$ Proteins. *Coordin. Chem. Rev.* **2014**, *280*, 54−83.
(69) Meyer, J. Iron−Sulfur Protein Folds, Iron−Sulfur Chemistry, and Evolution. *J. Biol. Inorg. Chem.* **2008**, *13*, 157−170.
(70) Mao, Z.; Liou, S.-H.; Khadka, N.; Jenney, F. E., Jr.; Goodin, D. B.; Seefeldt, L. C.; Adams, M. W.; Cramer, S. P.; Larsen, D. S. Cluster Dependent Charge-Transfer Dynamics in Iron-Sulfur Proteins. *Biochemistry* **2018**, *57*, 978−990.
(71) Vicente, J. B.; Teixeira, M. Redox and Spectroscopic Properties of the Escherichia Coli Nitric Oxide-Detoxifying System Involving Flavorubredoxin and Its NADH-Oxidizing Redox Partner. *J. Biol. Chem.* **2005**, *280*, 34599−34608.

DOI: 10.1021/acs.jctc.9b00641
J. Chem. Theory Comput. 2019, 15, 6074−6084

(72) Van Beilen, J. B.; Neuenschwander, M.; Smits, T. H.; Roth, C.; Balada, S. B.; Witholt, B. Rubredoxins Involved in Alkane Oxidation. *J. Bacteriol.* **2002**, *184*, 1722−1732.
(73) Nölling, J.; Ishii, M.; Koch, J.; Pihl, T. D.; Reeve, J. N.; Thauer, R. K.; Hedderich, R. Characterization of a 45-KDa Flavoprotein and Evidence for a Rubredoxin, Two Proteins That Could Participate in Electron Transport from H_2 to CO_2 in Methanogenesis in Methanobacterium Thermoautotrophicum. *Eur. J. Biochem.* **1995**, *231*, 628−638.
(74) Yoon, K.-S.; Hille, R.; Hemann, C.; Tabita, F. R. Rubredoxin from the Green Sulfur Bacterium Chlorobium Tepidum Functions as an Electron Acceptor for Pyruvate Ferredoxin Oxidoreductase. *J. Biol. Chem.* **1999**, *274*, 29772−29778.
(75) Chen, L.; Liu, M. Y.; Legall, J.; Fareleira, P.; Santos, H.; Xavier, A. V. Rubredoxin Oxidase, a New Flavo-Hemo-Protein, Is the Site of Oxygen Reduction to Water by the "Strict Anaerobe" Desulfovibrio Gigas. *Biochem. Biophys. Res. Commun.* **1993**, *193*, 100−105.
(76) Ma, K.; Adams, M. W. A Hyperactive NAD(P)H : Rubredoxin Oxidoreductase from the Hyperthermophilic Archaeon Pyrococcus Furiosus. *J. Bacteriol.* **1999**, *181*, 5530−5533.
(77) Calderon, R. H.; García-Cerdán, J. G.; Malnoë, A.; Cook, R.; Russell, J. J.; Gaw, C.; Dent, R. M.; de Vitry, C.; Niyogi, K. K. A Conserved Rubredoxin Is Necessary for Photosystem II Accumulation in Diverse Oxygenic Photoautotrophs. *J. Biol. Chem.* **2013**, *288*, 26688−26696.
(78) Heller, E. J.; Brown, R. C. Radiationless Transitions in a New Light. *J. Chem. Phys.* **1983**, *79*, 3336−3351.
(79) Tully, J. C. Collision Complex Model for Spin forbidden reactions: Quenching of $O(^1D)$ by N_2. *J. Chem. Phys.* **1974**, *61*, 61−68.
(80) Zahr, G. E.; Preston, R. K.; Miller, W. H. Theoretical Treatment of Quenching in $O(^1D) + N_2$ Collisions. *J. Chem. Phys.* **1975**, *62*, 1127−1135.
(81) Cui, Q.; Morokuma, K.; Bowman, J. M.; Klippenstein, S. J. The Spin-Forbidden Reaction $CH(^2\Pi)+N_2 \rightarrow HCN+N(^4S)$ Revisited. II. Nonadiabatic Transition State Theory and Application. *J. Chem. Phys.* **1999**, *110*, 9469−9482.
(82) Bearpark, M. J.; Robb, M. A.; Schlegel, H. B. A Direct Method for the Location of the Lowest Energy Point on a Potential Surface Crossing. *Chem. Phys. Lett.* **1994**, *223*, 269−274.
(83) Harvey, J. N.; Aschi, M.; Schwarz, H.; Koch, W. The Singlet and Triplet States of Phenyl Cation. A Hybrid Approach for Locating Minimum Energy Crossing Points between Non-Interacting Potential Energy Surfaces. *Theor. Chem. Acc.* **1998**, *99*, 95−99.
(84) Farazdel, A.; Dupuis, M. On the Determination of the Minimum on the Crossing Seam of Two Potential Energy Surfaces. *J. Comput. Chem.* **1991**, *12*, 276−282.
(85) Yarkony, D. R. Systematic Determination of Intersections of Potential Energy Surfaces Using a Lagrange Multiplier Constrained Procedure. *J. Phys. Chem.* **1993**, *97*, 4407−4412.
(86) Koga, N.; Morokuma, K. Determination of the Lowest Energy Point on the Crossing Seam between Two Potential Surfaces Using the Energy Gradient. *Chem. Phys. Lett.* **1985**, *119*, 371−374.
(87) Yarkony, D. R. Electronic Structure Aspects of Nonadiabatic Processes in Polyatomic Systems. In *Modern Electronic Structure Theory*; Yarkony, D. R., Ed., World Scientific: Singapore, 1995; pp. 642−721.
(88) Chachiyo, T.; Rodriguez, J. H. A Direct Method for Locating Minimum-Energy Crossing Points (MECPs) in Spin-Forbidden Transitions and Nonadiabatic Reactions. *J. Chem. Phys.* **2005**, *123*, No. 094711.
(89) Meilleur, F.; Munshi, P.; Robertson, L.; Stoica, A. D.; Crow, L.; Kovalevsky, A.; Koritsanszky, T.; Chakoumakos, B. C.; Blessing, R.; Myles, D. A. The IMAGINE Instrument: First Neutron Protein Structure and New Capabilities for Neutron Macromolecular Crystallography. *Acta Crystallogr., Sect. D: Biol. Crystallogr.* **2013**, *69*, 2157−2160.
(90) Pettersen, E. F.; Goddard, T. D.; Huang, C. C.; Couch, G. S.; Al, E. UCSF Chimera - a Visualization System for Exploratory Research and Analysis. *J. Comput. Chem.* **2004**, *25*, 1605−1612.
(91) Horn, H. W.; Swope, W. C.; Pitera, J. W.; Madura, J. D.; Dick, T. J.; Hura, G. L.; Head-gordon, T. Development of an Improved Four-Site Water Model for Biomolecular Simulations : TIP4P-Ew. *J. Chem. Phys.* **2004**, *120*, 9665−9678.
(92) Nishimoto, Y.; Fedorov, D. G. The Fragment Molecular Orbital Method Combined with Density-Functional Tight-Binding and the Polarizable Continuum Model. *Phys. Chem. Chem. Phys.* **2016**, 22047.
(93) Iikura, H.; Tsuneda, T.; Yanai, T.; Hirao, K. A Long-Range Correction Scheme for Generalized-Gradient-Approximation Exchange Functionals. *J. Chem. Phys.* **2001**, *115*, 3540−3544.
(94) Becke, A. D. Density-Functional Exchange-Energy Approximation with Correct Asymptotic Behavior. *Phys. Rev. A* **1988**, *38*, 3098−3100.
(95) Perdew, J. P.; Burke, K.; Ernzerhof, M. Generalized Gradient Approximation Made Simple. *Phys. Rev. Lett.* **1996**, *77*, 3865−3868.
(96) Weigend, F. Accurate Coulomb-Fitting Basis Sets for H to Rn. *Phys. Chem. Chem. Phys.* **2006**, *8*, 1057−1065.
(97) Nakata, H.; Fedorov, D. G.; Nagata, T.; Yokojima, S.; Ogata, K.; Kitaura, K.; Nakamura, S. Unrestricted Hartree-Fock Based on the Fragment Molecular Orbital Method: Energy and Its Analytic Gradient. *J. Chem. Phys.* **2012**, *137*, No. 044110.
(98) Binkley, J. S.; Pople, J. A.; Hehre, W. J. Self-Consistent Molecular Orbital Methods. 21. Small Split-Valence Basis Sets for First-Row Elements. *J. Am. Chem. Soc.* **1980**, *102*, 939−947.
(99) Gordon, M. S.; Binkley, J. S.; Pople, J. A.; Pietro, W. J.; Hehre, W. J. Self-Consistent Molecular-Orbital Methods. 22. Small Split-Valence Basis Sets for Second-Row Elements. *J. Am. Chem. Soc.* **1982**, *104*, 2797−2803.
(100) Dobbs, K. D.; Hehre, W. J. Molecular Orbital Theory of the Properties of Inorganic and Organometallic Compounds 4. Extended Basis Sets for Third-and Fourth-Row, Main-Group Elements. *J. Comput. Chem.* **1986**, *7*, 1986.
(101) Nakata, H.; Fedorov, D. G.; Yokojima, S.; Kitaura, K.; Sakurai, M.; Nakamura, S. Unrestricted Density Functional Theory Based on the Fragment Molecular Orbital Method for the Ground and Excited State Calculations of Large Systems. *J. Chem. Phys.* **2014**, *140*, 144101.
(102) Ditchfield, R.; Hehre, W. J.; Pople, J. A. Self-Consistent Molecular-Orbital Methods. IX. An Extended Gaussian-Type Basis for Molecular-Orbital Studies of Organic Molecules. *J. Chem. Phys.* **1971**, *54*, 724−728.
(103) Rassolov, V. A.; Pople, J. A.; Ratner, M. A.; Windus, T. L.; Rassolov, V. A.; Pople, J. A.; Ratner, M. A.; Windus, T. L. 6-31G* Basis Set for Atoms K through Zn. *J. Chem. Phys.* **2003**, *109*, 1223−1229.
(104) Stewart, J. J. P. Optimization of Parameters for Semiempirical Methods VI: More Modifications to the NDDO Approximations and Re-Optimization of Parameters. *J. Mol. Model.* **2013**, *19*, 1−32.
(105) MOPAC2016; Stewart, J. J. Stewart Computational Chemistry. *J. Nucl. Fuel Cycle Environ.* Colorado Springs, CO, USA. 1998, *5*, 73−79.
(106) Nakata, H.; Fedorov, D. G.; Kitaura, K.; Nakamura, S. Extension of the Fragment Molecular Orbital Method to Treat Large Open-Shell Systems in Solution. *Chem. Phys. Lett.* **2015**, *635*, 86−92.
(107) Tomasi, J.; Mennucci, B.; Cammi, R. Quantum Mechanical Continuum Solvation Models. *Chem. Rev.* **2005**, *105*, 2999−3094.
(108) Cossi, M.; Rega, N.; Scalmani, G.; Barone, V. Energies, Structures, and Electronic Properties of Molecules in Solution with the C-PCM Solvation Model. *J. Comput. Chem.* **2003**, *24*, 669−681.
(109) Fedorov, D. G.; Olson, R. M.; Kitaura, K.; Gordon, M. S.; Koseki, S. A New Hierarchical Parallelization Scheme: Generalized Distributed Data Interface (GDDI), and an Application to the Fragment Molecular Orbital Method (FMO). *J. Comput. Chem.* **2004**, *25*, 872−880.
(110) Mironov, V; Alexeev, Y; Fedorov, D. G.; Umeda, H.; Pruitt, S.; Gaenko, A.; Gordon, M. S. Multi- Level Parallelization of the

DOI: 10.1021/acs.jctc.9b00641
J. Chem. Theory Comput. 2019, 15, 6074−6084

Fragment Molecular Orbital Method in GAMESS. In *Recent advances of the fragment molecular orbital method*; Springer Japan: Tokyo, 2019.
(111) Nakano, T.; Kaminuma, T.; Sato, T.; Fukuzawa, K.; Akiyama, Y.; Uebayasi, M.; Kitaura, K. Fragment Molecular Orbital Method: Use of Approximate Electrostatic Potential. *Chem. Phys. Lett.* **2002**, *351*, 475−480.
(112) Alexeev, Y.; Mahajan, A.; Leyffer, S.; Fletcher, G.; Fedorov, D. G. Heuristic Static Load-Balancing Algorithm Applied to the Fragment Molecular Orbital Method. In *International Conference for High Performance Computing, Networking, Storage and Analysis, SC*; Salt Lake City, Utah, USA, 2012.
(113) Mironov, V.; Alexeev, Y.; Fedorov, D. G. Multithreaded Parallelization of the Energy and Analytic Gradient in the Fragment Molecular Orbital Method. *Int. J. Quantum Chem.* **2019**, *119*, 1−14.
(114) Vuong, V. Q.; Nishimoto, Y.; Fedorov, D. G.; Sumpter, B. G.; Niehaus, T. A.; Irle, S. The Fragment Molecular Orbital Method Based on Long-Range Corrected Density-Functional Tight-Binding. *J. Chem. Theory Comput.* **2019**, *15*, 3008−3020.

DOI: 10.1021/acs.jctc.9b00641
J. Chem. Theory Comput. 2019, 15, 6074−6084